NeuroImage **12,** 676–687 (2000)
doi:10.1006/nimg.2000.0666, available online at http://www.idealibrary.com on IDEAL®

Bayesian Construction of Geometrically Based Cortical Thickness Metrics

Michael I. Miller, Allan B. Massie, J. Tilak Ratnanather, Kelly N. Botteron,* and John G. Csernansky*

Center for Imaging Science, The Johns Hopkins University, Charles and 34th Street, Baltimore, Maryland 21218-2686; and
**Department of Psychiatry, Washington University School of Medicine, St. Louis, Missouri 63110*

Received March 9, 2000

This paper describes the construction of cortical metrics quantifying the probabilistic occurrence of gray matter, white matter, and cerebrospinal fluid compartments in their correlation to the geometry of the neocortex as measured in 0.5–1.0 mm magnetic resonance imagery. These cortical profiles represent the density of the tissue types as a function of distance to the cortical surface. These metrics are consistent when generated across multiple brains indicating a fundamental property of the neocortex. Methods are proposed for incorporating such metrics into automated Bayes segmentation. © 2000 Academic Press

INTRODUCTION

One of the most striking macroscopic features of mammalian neuroanatomy is the gyral and sulcal patterning of the neocortex. Computational anatomists have been studying the shape and folding of the neocortex as well as the cortical mantle volume, thickness, and density directly, as the mantle is an important indicator of gray matter properties. At the macroscopic scale of 0.1–1 mm, which is currently routinely available via noninvasive imaging technologies, automated methods are being developed to aid the anatomist in constructing a 3-dimensional (3-D) volume representation of the cortical mantle, as well as a 2-dimensional (2-D) surface representation of the gray/white matter cortical surface and the midlayer 4 surface (see Dale and Sereno, 1993; Kapur *et al.*, 1996; Thompson *et al.*, 1996; Drury *et al.*, 1996; van Essen *et al.*, 1998; Valliant and Davatzikos, 1997; Teo *et al.*, 1997; Bakircioglu *et al.*, 1998; Miller *et al.*, 1998; Bakircioglu *et al.*, 1999; Joshi *et al.*, 1999, and the recent book of Toga, 1999, for example). In all approaches, there are two central components to the analysis of the neocortex: (i) the construction of the 3-D neocortical mantle representing the positions of the gray matter connected voxels forming a highly curving structure, and (ii) the construction of a polygonal (perhaps triangulated) graph representing the 2-dimensional manifold of the midlayer 4 boundary, the gray/white matter boundary, or the gray/CSF boundary. These two components (i) and (ii) are linked in that the 2-dimensional manifold of the surface, and therefore its curving geometry, are determined by the variation, position, and density of the cortical mantle cells, manifested as gray matter at the macroscopic scale of current MRI imaging methods.

This intrinsic coupling forms the basis for the principal focus of this paper, the construction of *frequency of occurrence metrics* describing the 3-D neocortical mantle density and covariation of surrounding compartments, gray matter (G), white matter (W), and cerebrospinal fluid (CSF) spaces. We define metrics which are empirically constructed from the relative frequency of occurrence of the tissue compartments as a function of the associated 2-dimensional cortical manifold representing the cortical mantle. Herein these metrics are constructed for several gyri, including the prefrontal, cingulate, and superior temporal gyri. The metrics are treated as homogeneous across gyri; in general they should be expected to be indexed relative to their position in the cortical surface.

We present the methods for generating frequency of occurrence metrics on the covariation of the G, W, CSF compartments in 3-D MRI brain images as a function of location in the image with respect to the cortical surface geometry. Such probabilistic information characterizes statistical variations in the 3-D cortical mantle as manifested by density, volume, and thickness changes. Results from 14 human MRI-imaged gyrus volumes are shown.

METHODS

Bayes Segmentation and the Cortical Surface

Bayes segmentation. To construct the surface and volume segmentations we follow the procedure of Teo *et al.* (1997) and extended by Joshi *et al.* (1999) to

1053-8119/00 $35.00

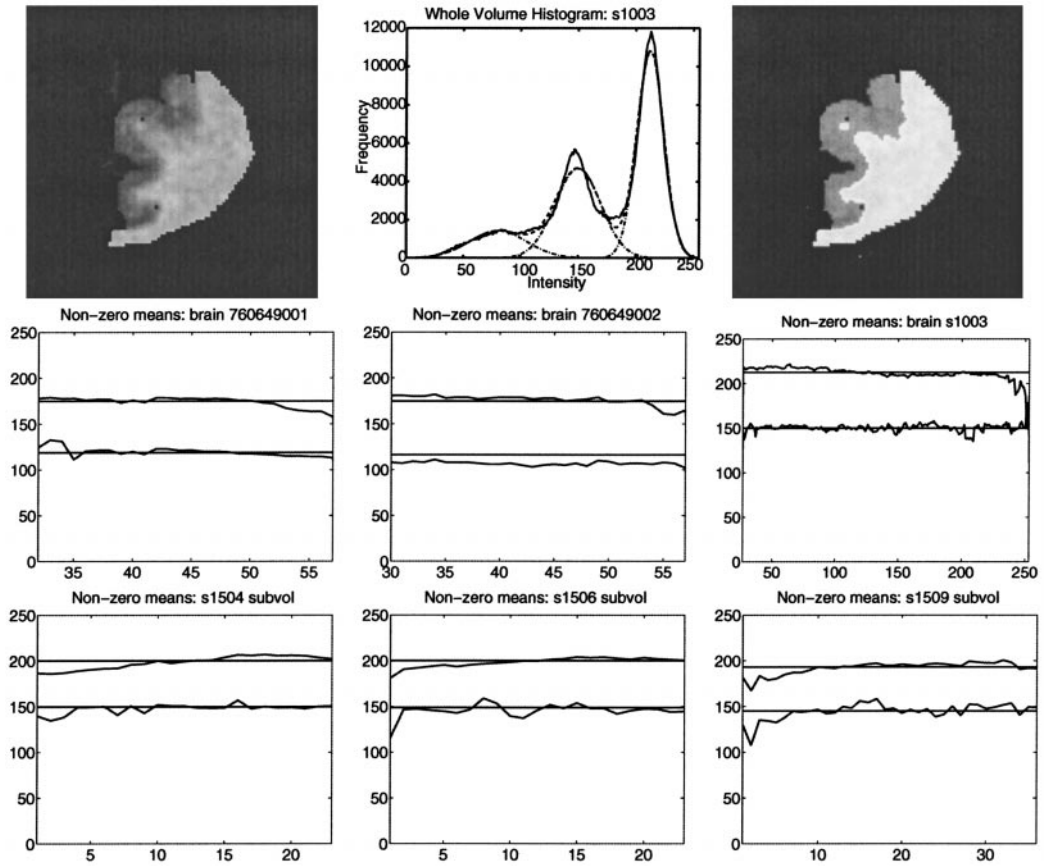

FIG. 1. Top row shows parametric fits for subvolume s1003 for coronal section 135. Middle and bottom rows show the mean of G, W compartments empirically estimated using the EM algorithm fitting as a function of section number. The straight lines are the G, W parameters estimated from the single histograms of the entire gyrus cube. Middle row shows data from the prefrontal gyrus 760649001, 760649002, and cingulate gyrus 1003. Horizontal axes show the coronal slice number and the vertical axes the intensity values. Bottom row shows data from a subvolume of the temporal gyrus 1504, 1506, 1509. Data taken from the laboratories of Drs. Kelly Botteron and John Csernansky, Washington University.

accommodate tissue variation via mixture densities representing the gray, white, and CSF tissue types. Local recalibration is accomplished via the expectation-maximization (EM) algorithm (Joshi *et al.*, 1999) for fitting of the parameters of the mixture densities throughout the brain data, analogous to that in Kapur *et al.* (1996). To study the geometry of gyrification, surfaces are generated to fit the gray/white matter interface using isocontouring and active surface methods. We follow the procedure of Joshi *et al.* (1999). Define image $I : \Omega \rightarrow \mathbb{R}^m$ a (perhaps vector-valued) function for multiple modalities defined on the coordinates $x \in \Omega$. Assume that Ω is a discrete lattice, with x_n, $n = 1, \ldots, N$ discrete voxels making up the coordinates of the image volume. Associate with each image I an anatomical label. Define $h \in \mathcal{H}$ the space of anatomical labelings of the entire image, so that

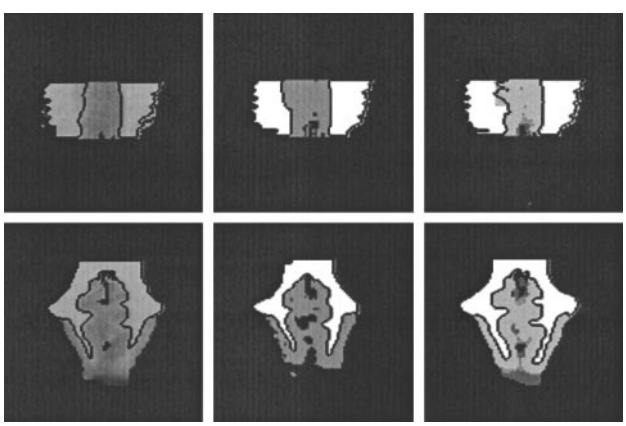

FIG. 2. Rows 1 and 2 show the brain 760649002 in axial and coronal views. Column 1 shows the embedding of the reconstructed surface in the whole brain MRI image volumes. Column 2 shows the embedding in the automated segmentation. Column 3 shows the hand segmentation for comparison. Data taken from the laboratory of Dr. Kelly Botteron at Washington University.

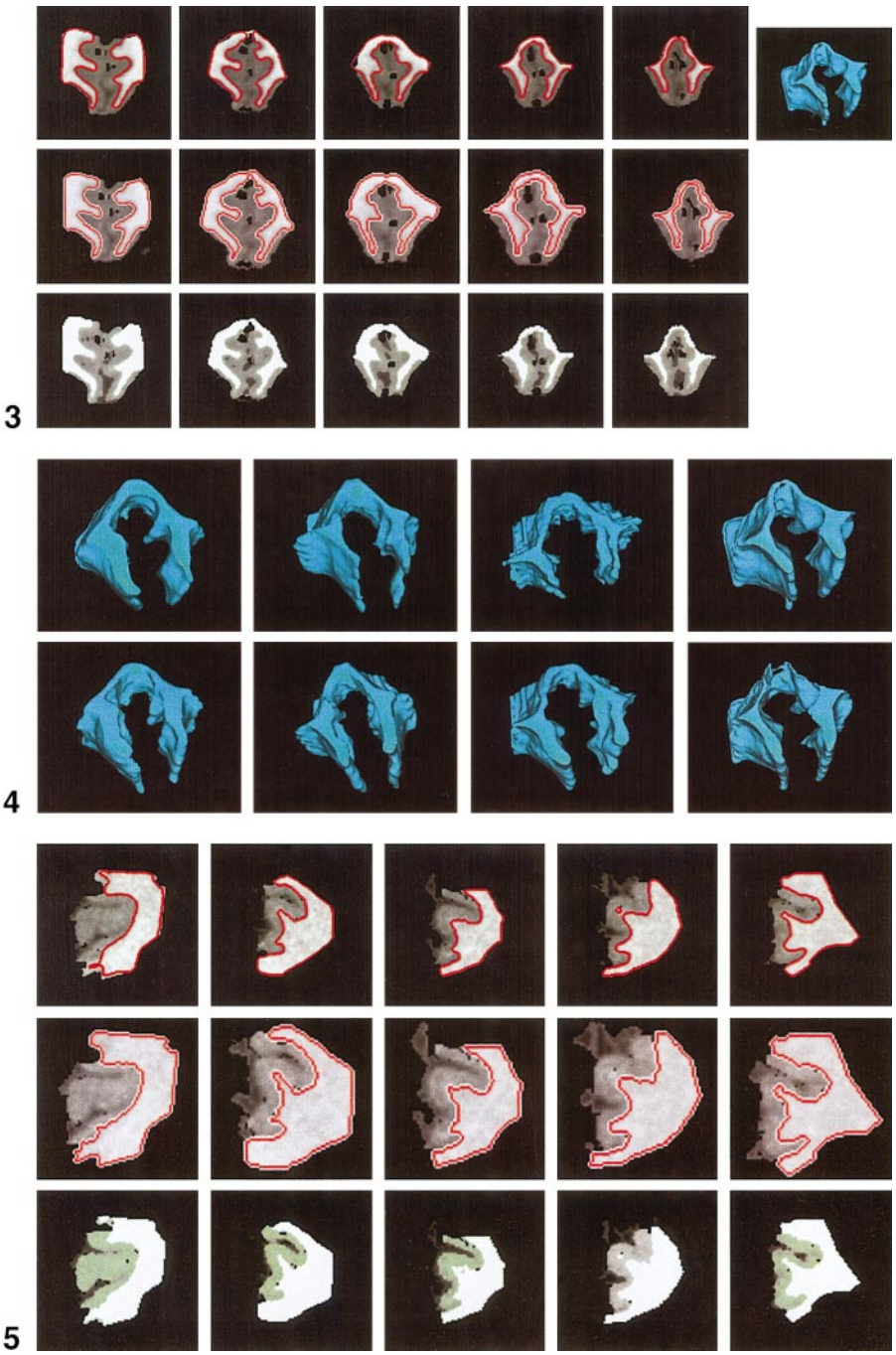

FIG. 3. Figure shows coronal sections of prefrontal gyrus 770613002 showing sections 26, 31, 44, 51, and 57. Top row shows the MRI brain image with embedded surface. Middle row shows the hand-generated contours embedded in the image. Bottom row shows the G, W, CSF segmentation overlaying the original image. The extreme right panel shows the associated surface reconstructed from the segmentations. Data taken from the laboratory of Dr. Kelly Botteron.

FIG. 4. Top row shows surfaces for the prefrontal gyrus generated via the automated segmentation and isocontouring algorithm. Bottom row shows the same generated from the hand segmented volumes. Data taken from the laboratory of Dr. Kelly Botteron of Washington University.

FIG. 5. Coronal sections 30, 70, 100, 135, 172 from brain s1003 generated in the laboratory of Dr. John Csernansky. Top row shows the automatically constructed embedded surface in the image volume. Middle row shows the hand-generated contours embedded in the image volume for comparison. Bottom row shows the automated segmentation into G, W compartments.

TABLE 1

The L_1 Distances between the Bayesian Segmentation and Hand Segmentation of MRI Volumes for Estimating G, W, CSF Compartments

Brain	PF1	PF2	PF3	PF4	PF5	C1	C2	C3	T1	T2	T3	T4	D1	D2
Distance	0.10	0.11	0.18	0.10	0.10	0.06	0.09	0.12	0.12	0.18	0.16	0.14	0.10	0.10

Note. The first row shows the names of the brains. The second row shows the distances for section by section fitting of the means and variances. The first five PF brains correspond to MRIs of the prefrontal gyrus; the next three C brains were taken from the cingulate gyrus; the next four T brains were taken from the superior temporal gyrus; and the last two D brains were taken from a subvolume of the superior temporal gyrus. Hand segmentations for the prefrontal gyrus were performed in the laboratory of Dr. Kelly Botteron; for the cingulate gyrus they were performed in the laboratory of Dr. John Csernansky. The hand segmentations of the superior temporal gyrus brains were done in our lab.

$$h \stackrel{\Delta}{=} \{h_n,\ n = 1, \ldots, N,\ h \in \text{MODEL} - \text{TYPES}\}. \tag{1}$$

Assume the simple statistical mixture model of conditional Gaussian data for I with compartment types MODEL − TYPES = $\{G, W, CSF\}$, representing gray matter, white matter, and cerebrospinal fluid, respectively, with means and variances μ_n, σ_n^2 a function of position $n = 1, \ldots, N$. Joshi *et al.* (1999) estimates μ_n, σ_n^2 locally as a function of position in the lattice so that the posterior-probability becomes

$$p(h|I) = \prod_{n=1}^{N} \frac{1}{\sqrt{2\pi\sigma_n^2(h_n)}}\, e^{-(I_n-\mu_n(h_n))^2/2\sigma_n^2(h_n)}\pi(h), \tag{2}$$

with $\pi(h)$ the prior distribution representing the relative amount of G, W, CSF compartments in the section. The optimal Bayes maximum a-posteriori segmentation of Joshi *et al.* (1999) for $\pi(h)$ conditionally independent over voxels generates the labels according to the following:[2]

$$\begin{aligned}\text{for each } l,\ \hat{h}_n &= \arg\max_{h_n \in \mathcal{H}} \log p(h_n|I);\\ &= \sum_{n=1}^{N}\left(-\frac{1}{2}\log 2\pi\sigma_n^2(h_n)\right.\\ &\quad\left.-\frac{1}{2}\frac{(I_n-\mu_n(h_n))^2}{\sigma_n^2(h_n)} + \log \pi(h_n)\right)\end{aligned} \tag{3}$$

An example demonstrating the semiautomated calibration fits is shown in Fig. 1. The top row shows the parameters for the G, W, CSF compartments of cingulate gyrus. The left panel shows the image data, the middle panel shows the sample fit via the EM algorithm to the histogram, and the right panel shows the segmented volume. The middle and bottom rows of Fig. 1 show the empirical estimates of the mean G, W compartment parameters estimated using the EM algorithm fitted as a function of section number from six of the gyri measured with whole brain MRI. The middle row shows data from the prefrontal gyrus (panels 1, 2) and cingulate gyrus (panel 3) from the laboratories of Drs. Kelly Botteron and John Csernansky, respectively. The bottom row shows data from the superior temporal gyrus. As is evident from the data, the variation of mean parameters is small over the volumes. This is consistent with our findings for MRI data which has been acquired with the most modern pulse sequences.

Surface generation. Once the statistics are estimated empirically, then the whole brain volumes are segmented using these statistics μ_n, σ_n^2 to locally fit the compartmental statistics using the Bayes segmentation algorithm. From the local parametric mixture model segmentation, isosurface generation is used to generate the triangulated graphs representing the cortical surface. For generating triangulated surfaces we use the isosurface generation algorithm by Gueziec and Hummel (1995) that uses tetrahedral decomposition. This algorithm is similar to the "Marching Cubes" algorithm (Lorensen and Cline, 1987). The "Marching Cubes" algorithm has some inherent ambiguities that can result in surfaces that contain holes. The tetrahedral decomposition algorithm generates a tessellation of triangles for an isosurface of a given intensity. It decomposes each voxel (eight points) into five tetrahedra. The resulting surface is a triangulation made up of the triangles that bound these tetrahedra. This algorithm is used for all of the surfaces shown presented in this paper.

Shown in Fig. 2 are example embeddings of the generated surfaces in the image volumes and segmentations for the prefrontal gyrus. The figure shows axial (row 1) and coronal (row 2) sections of brain 760649002. Column 1 shows the embedding of the re-

[2] Assumed throughout are equal costs between incorrect hypotheses with zero-cost for correct hypotheses thus giving the thresholds associated with the maximum a-posteriori probability choice. As originally proposed in Joshi *et al.* (1999) are the flexibility to introduce unequal costs.

TABLE 2

The CSF, G, W Compartment Volumes in mm^3 Generated from the Automated and Hand Segmentations of the Prefrontal and Cingulate Gyrus Volumes and Superior Temporal Gyrus Subvolumes, with the Difference in mm^3 between the Volumes of the Compartments in the Hand and Auto Segmentations

Brain name	Auto			Hand			Difference		
	CSF	GM	WM	CSF	GM	WM	CSF	GM	WM
760649001	752.62	3190.00	3121.12	1016.25	3054.38	2993.12	−263.63	135.62	128.00
760649002	869.75	3460.12	3162.50	759.94	3386.56	3345.88	109.81	73.56	−183.38
770613001	1198.50	3238.50	2585.88	1015.38	3275.12	2732.38	183.12	−36.62	−146.50
770613002	739.12	4790.25	3609.62	715.06	4814.31	3609.62	24.06	−24.06	0.00
770632001	504.38	2171.38	2848.88	487.88	2335.25	2701.50	16.50	−163.87	147.38
s1003	12762.38	21789.75	44986.62	11254.38	23316.12	44968.25	1508.00	−1526.37	18.37
s2002	6805.38	18839.25	23647.25	5713.62	19374.12	24204.12	1091.76	−534.87	−556.87
s2003	14708.38	27068.12	34529.50	13577.12	22692.25	40036.62	1131.26	4375.87	−5507.12
Damasio1	4896.25	38200.00	30803.75	5356.25	39045.00	29498.75	−440.00	−845.00	1305.00
Damasio2	11172.50	39021.25	33135.00	10010.00	39937.50	33381.25	1162.50	−916.25	−246.25

Note. The automated segmentation was performed with a single set of mean and variance values for entire gyrus volumes. Prefrontal gyri were measured in the laboratory of Dr. Kelly Botteron from Washington University; the cingulate gyri were measured in the laboratory of Dr. John Csernansky from Washington University.

constructed surface in the whole brain MRI image volumes. Column 2 shows the embedding of the surface in the automated segmentation that it was generated from. Column 3 shows for comparison a surface generated from the hand generated segmentation, embedded in that segmentation. Data was taken from the laboratory of Dr. Kelly Botteron at Washington University.

Shown in Fig. 3 are a series of coronal sections for the pre-frontal gyrus 770613002. The top row shows the MRI brain image with the embedded surface depicted at the intersection of G, W compartments. The middle row shows the hand-generated contours at the G, W boundary in each of the sections for purpose of comparison. The bottom row shows the Bayes segmentation which were used for generating the surface shown embedded in the top row.

Figure 4 shows the surfaces generated from the prefrontal gyrus. The top row shows four surfaces for the prefrontal gyrus generated via the automated segmentation and isocontouring algorithm for four brains. The bottom row shows the four surfaces generated from the hand segmentations of the prefrontal cortex. Notice the similarity of the reconstructed surfaces.

Figure 5 shows coronal cross sections of cingulate gyrus s1003, with the solid line contours depicting the intersection of the automatically generated embedded surface with the subsection. The top row shows sections of the MRI image volume. The middle row shows the contours hand-generated at the G, W boundary in each of the sections for purpose of comparison. The bottom row shows the automatically generated segmentation overlaying the original MRI image which were used to generated the surface shown embedded in the top row.

Empirical Constructions of Cortical Thickness Metrics

We now describe methods for generating frequency of occurrence metrics of the cortical thickness, and of the occurrence of G, W, CSF compartments in MRI brain images as a function of cortical location. These metrics characterize the statistical frequency of occurrence of the three G, W, CSF compartments in MRIs of the neocortex. First a surface S is generated, which separates the G, W compartments. Then a boundary "shell" of voxels is constructed, which intersect the surface, marking all voxels in the filled region as interior voxels, and all voxels not in the boundary as exterior. For each exterior voxel, we compute the distance to the surface. Voxels in the boundary shell are considered to have a distance of zero from the surface. Histograms of G, W, CSF frequency of occurrence as a function of distance to the surface are calculated, maintaining separate histograms for G, W, CSF voxels. Using these histograms, we can compute the probability that a voxel at a given distance from the surface is G, W, CSF.

We denote these empirically generated probabilities as $\pi(h_n|S)$, the probability of tissue type $h_n \in \{G, W, CSF\}$ occurring in voxel x_n on the given surface S. We shall assume throughout that these prior distributions are homogeneous over a complete gyrus and only a function of the distance $d(x_n, S)$ between voxel x_n and the surface, d being the set distance

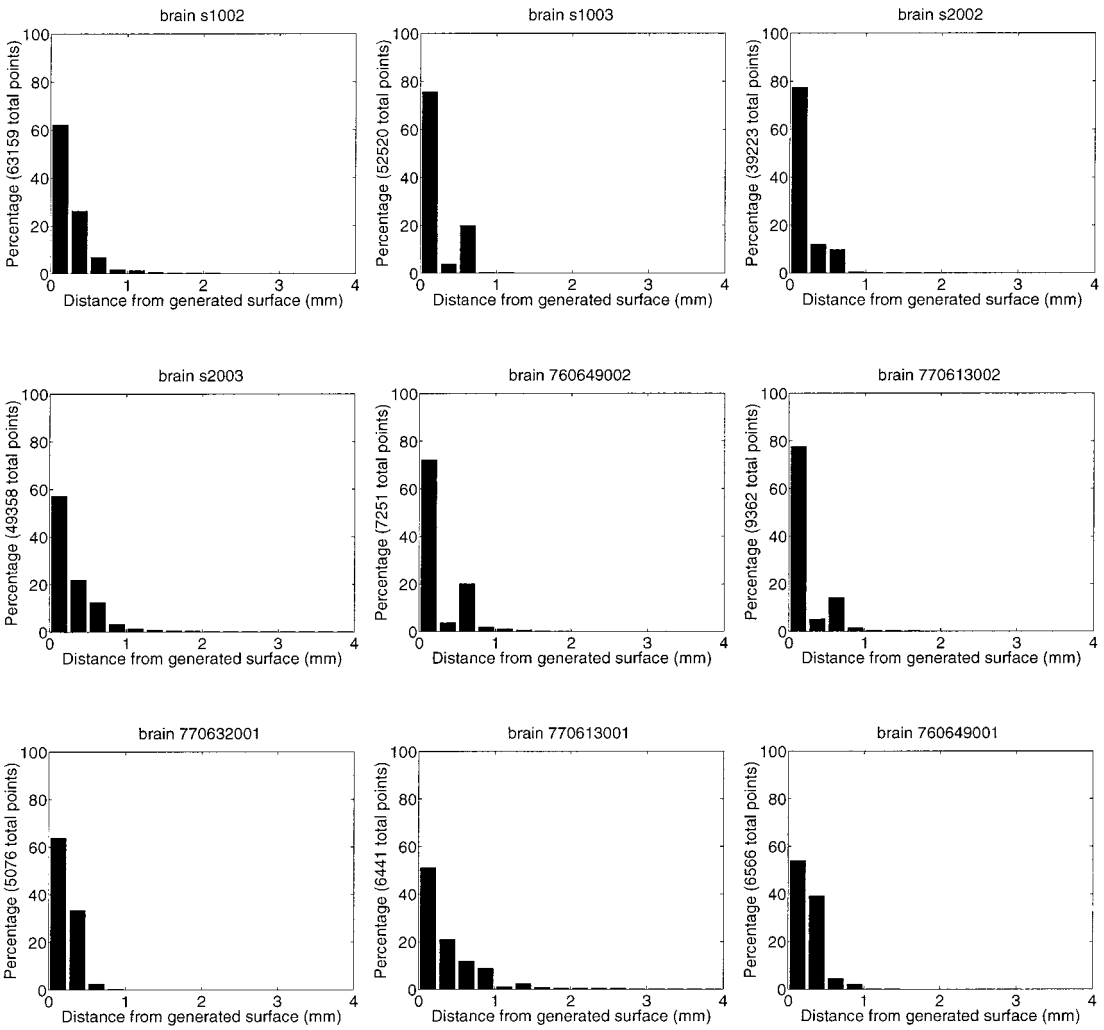

FIG. 6. Figures show the L_1 distances between the hand-generated contours and the automatically generated surfaces in the nine brain MRI subvolumes.

$$d(x_n, S) = \min_{s \in S} d(x_n, s). \tag{4}$$

The surface nodes and image voxel nodes do not fall on the same grid. Therefore for all of the distances standard interpolation to center points of the voxel and the triangles are computed. Since both the number of voxels in the image space and the number of vertices in the surface are very large, it is time-consuming to compute the distance between every voxel and every vertex in the surface. Therefore, it is useful if we can examine only a subset of the surface vertices and still determine the distance from every voxel to the surface. For that reason, to compute the distances, we do not measure the distance between every voxel in the image and every vertex in the surface. Instead, we begin by placing the vertices into nx linked lists, where nx is the X-dimension of the image in voxels, with each list corresponding to one x-plane. To find the closest vertex to a voxel with x-coordinate x_i, we measure the distance between the voxel and each vertex in the list corresponding to plane x_i. We then do the same with $x_i - 1$, $x_i - 2$, . . . until the distance between plane x_i and the current plane is greater than the distance to the closest vertex found so far. Next we examine plane $x_i + 1$, etc., until the distance between planes exceeds the distance to the closest vertex found so far. This vertex is the closest vertex to the voxel.

That is described by the following algorithm:

Algorithm 1 (Distance Computation Algorithm)

1. Preprocessing: define nx subsurfaces by:

$$S_i \triangleq \{p \in S \mid \lfloor p \cdot x \rfloor = i\},\ 0 \le i < nx; \tag{5}$$

2. Given a voxel center c, set $i = \lfloor c \cdot x \rfloor$, $j = i - 1$, $k = i + 1$:

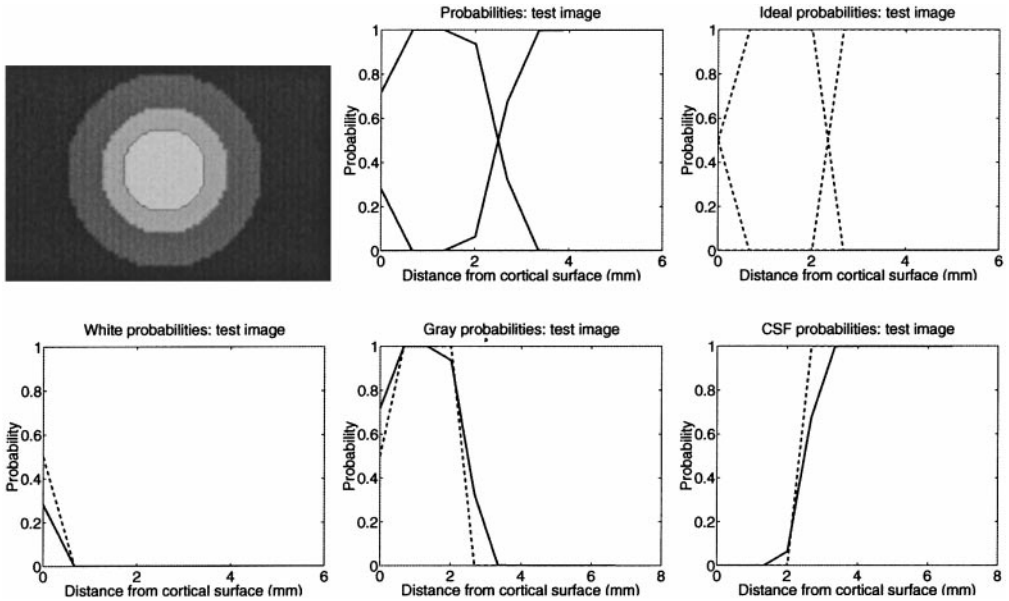

FIG. 7. Left panel shows a cross-section of the 3-dimensional phantom, illustrating gray, white, CSF compartments. Middle panel shows the calculated probabilities of G, W, CSF as a function of distance from the G, W surface boundary. Right panel shows the ideal profile of G, W, CSF over distance. Bottom panels show ideal (dashed line) and computed (solid line) probabilities superimposed, for G, W, CSF, respectively. In this phantom image, the length of one voxel is considered 1 mm.

$$p_{\min} = \arg\min_{p \in S_i}\{\mathrm{d(c,\ p)}\}; \tag{6}$$

3. While (($j > 0$ or $k < nx$) and $|i - j| < d(p_{\min,c})$):

$$p(j) = \arg\min_{\mathrm{p}\in \mathrm{S_j}}\{d(c,\ p)\} \tag{7}$$

$$p(k) = \arg\min_{\mathrm{p}\in \mathrm{S_k}}\{d(c,\ p)\} \tag{8}$$

If $d(p(j), c) < d(p_{\min}, c)$ then $p_{\min} = p(j)$;
If $d(p(k), c) < d(p_{\min}, c)$ then $p_{\min} = p(k)$
$j = j - 1$, $k = k + 1$

RESULTS AND DISCUSSION

Quantifying Segmentation Accuracy

Joshi *et al.* (1999) examined the reliability of the Bayes mixture segmentation as compared to hand segmentations in the macaque. We have done the same here for the MRI volumes, in which all of the volumes were hand segmented. The prefrontal gyri were collected and hand segmented in Dr. Kelly Botteron's laboratory at Washington University. The cingulate gyri were collected and hand segmented in Dr. John Csernansky's laboratory at Washington University. For comparison we use the L_1 distance between hand and automated segmentations.

Assume an image contains N voxels, and let $\mathcal{M}$ be a manual segmentation of the image such that each of the M compartments is labeled with a tag from 1 to M (zero represents areas of the volume which are not segmented, for instance the background). Suppose that $\mathcal{A}$ is an M compartment automated segmentation with the same labeling scheme as the reference manual segmentation. To measure agreement over a particular compartment or union of compartments in M, let $p(h_n|I)$ be the a posteriori probability of hypothesis h_n occurring at voxel n, and let $p^{\mathcal{M}}(h_n|I)$ be the posteriori probability of hypothesis h_n at voxel n for the manual segmentation. Generally, this will have a value of either 1 or 0, unless the manual rater assigns partial volume numbers to the compartment. The estimate of the average L_1 distance between the two segmentations over the set of interest becomes

$$\frac{1}{N}\sum_{n=1}^{N}\sum_{m=1}^{M}|p(h_n = H_m|I) - p^{\mathcal{M}}(h_n = H_m|I). \tag{9}$$

Shown in Table 1 are the results of automated segmentations compared to hand segmentations. Notice across all of the gyri upwards of about 90% agreement are obtained. The first five correspond to the prefrontal gyri from Dr. Botteron at Washington University, the next three to the cingulate gyri from Dr. Csernansky at Washington University, the last four to subvolumes of the superior temporal gyrus measured at Washington University, and the last two to brains from Dr. Damasio at the University of Iowa.

Table 2 shows the segmentation volumes of the G, W, CSF compartment volumes generated from the auto-

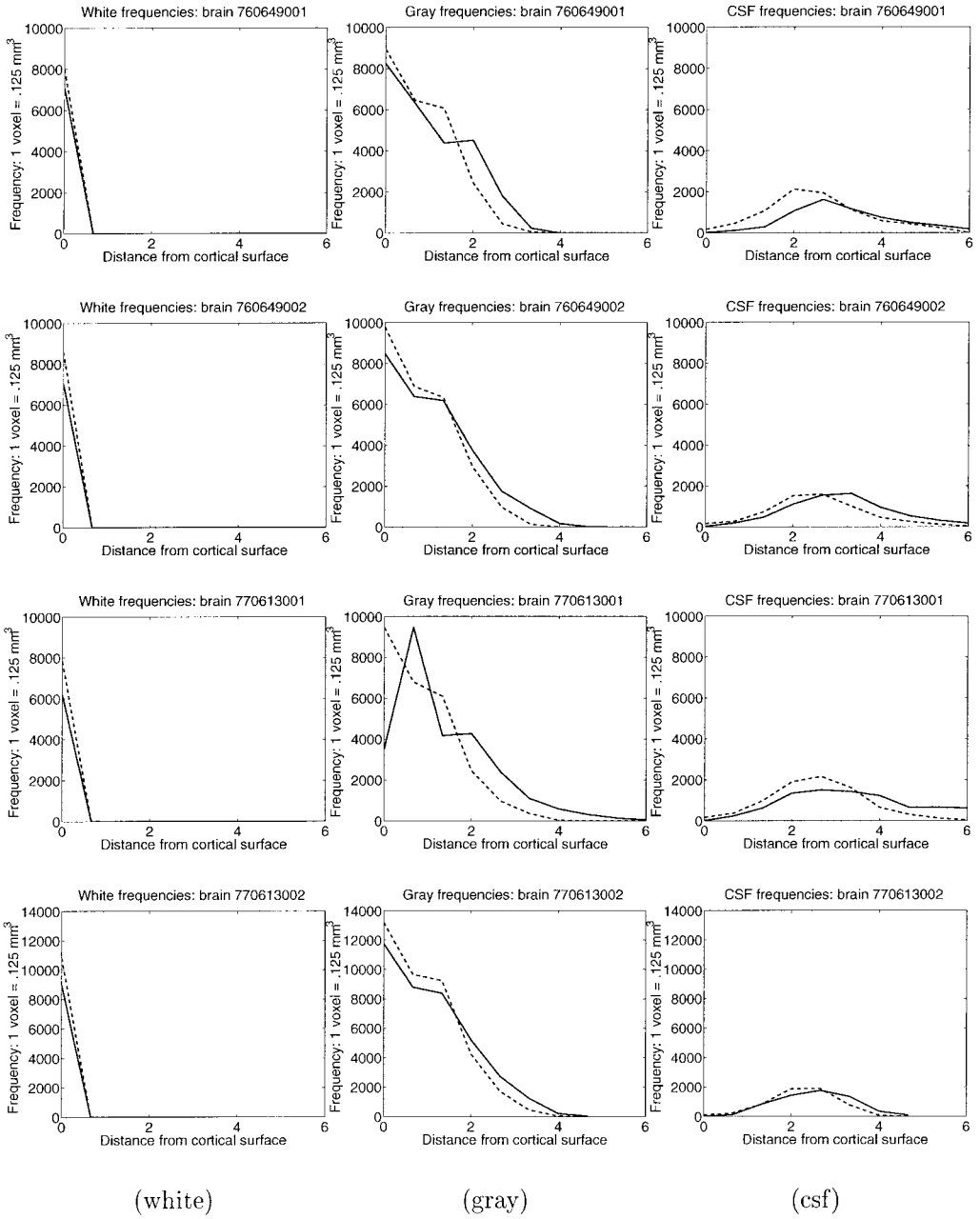

FIG. 8. Figure shows frequency of occurrence comparison of hand segmentation (dashed line) and automated segmentation (solid line) of white, gray, CSF compartments generated from auto segmentations. Distances from the cortical surface are in mm. Rows 1–4 show prefrontal gyri.

mated and hand segmentations of the prefrontal, cingulate, and the superior temporal gyrus. Notice the excellent agreement between the hand segmentation volumes and the automated segmentation volumes.

Validating Surface Generation

To examine the accuracy of the automatically generated triangulated graph surfaces the set of brains were hand contoured. The hand drawn contours are generated using the Analyze software (http://www.mayo.edu/bir/), and were generated at the interface of G, W matter boundary in each of the sections in each of the brain. These hand generated contours are taken as the gold standard to which the automatic surface generation is compared. Shown in the middle rows of Figs. 3 and 5 are examples of embedded contours generated via hand contouring of two of the MRI subvolumes. Notice the excellent visual correspondence between the

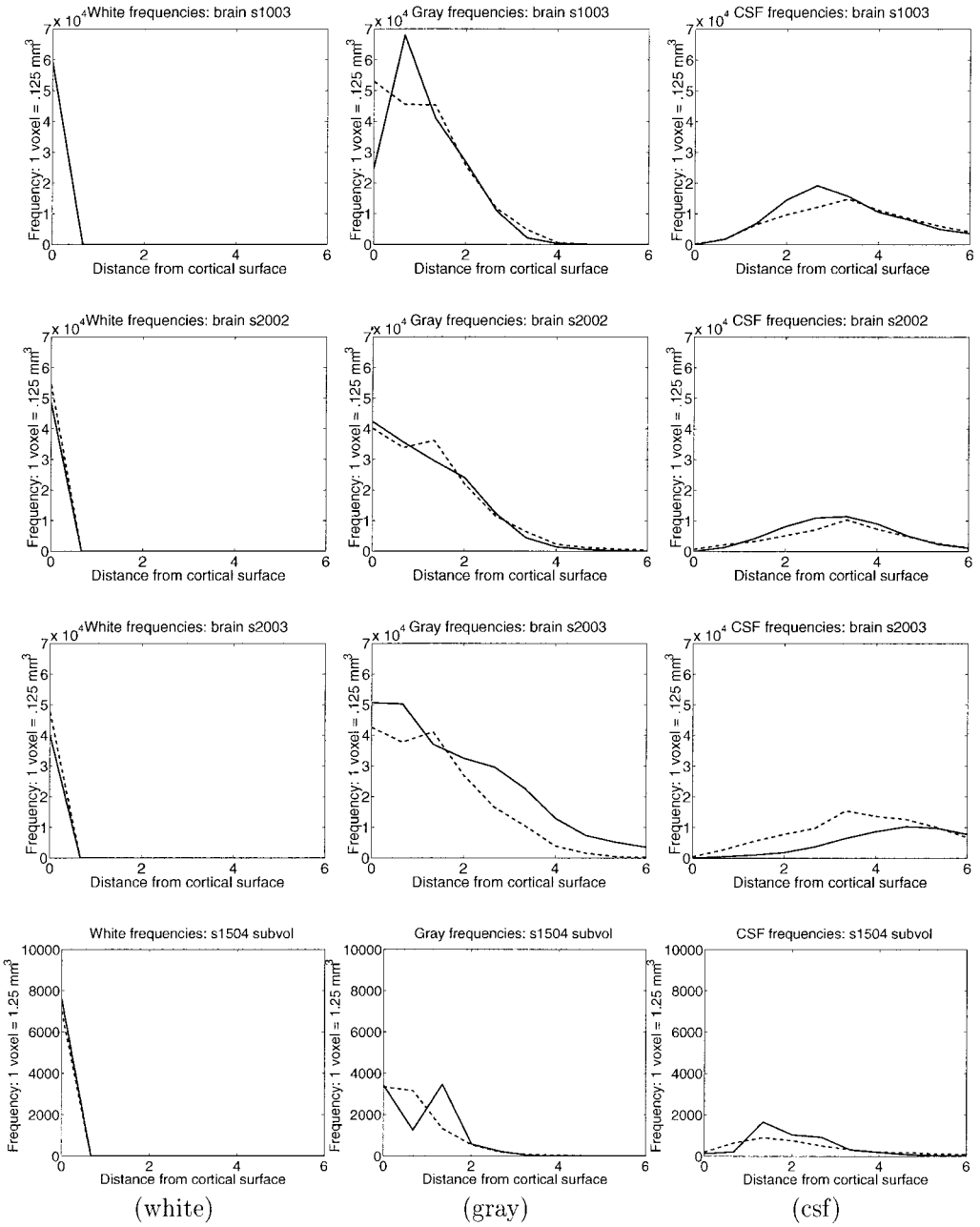

FIG. 9. Figure shows frequency of occurrence comparison of hand segmentation (dashed line) and automated segmentation (solid line) of white, gray, CSF compartments generated from auto segmentations. Distances from the cortical surface are in mm. Rows 1–3 show cingulate gyri. Row 4 shows the superior temporal gyrus.

generated embedded surface and the hand generated contours.

To validate the isosurface generation over all of the MRI brain volumes, these hand-generated contours are compared to the embedded surfaces. For each vertex on every contour a distance is calculated between it and the automatically generated isosurfaces constructed from the Bayes segmentation. These distances are generally in fractions of voxels. For each brain a histogram of distances are calculated. Shown in Fig. 6 are the histogram of distances calculated for the nine brains which were hand contoured.

Cortical Thickness Metrics

Travelling normal to the surface, white matter, gray matter and CSF occur in amounts that vary with the distance from the cortical surface. To compute the em-

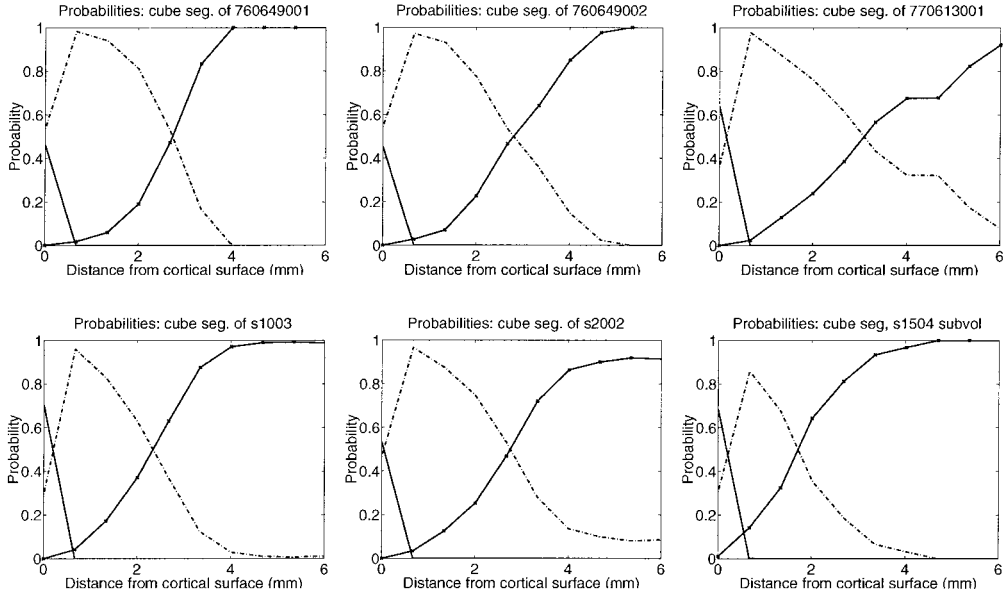

FIG. 10. Figure shows conditional probabilities of occurrence of white, gray, CSF compartments as a function of millimeter distance from the gray/white matter boundary. The solid, dashed, and cross-hatched lines represent white matter, gray matter, and CSF, respectively. Top row shows three prefrontal gyri analyzed from the laboratory of Dr. Kelly Botteron of Washington University. Bottom row show two cingulate gyri and one superior temporal gyrus from the laboratory of Dr. John Csernansky of Washington University. Distances from the cortical surface are in mm.

pirical covariation of the G, W, CSF compartments, we calculate by the above algorithm the relative frequency of each compartmental hypothesis. This gives a metric of density of each compartment as a function of distance from the surface. Figure 7 shows a phantom constructed to verify the method. Panel 1 shows a section through a series of concentric spheres modelling the gray/white/CSF compartments. The surface is defined at the interface of the gray/white compartments. Panels 2 and 3 show the exact probability profiles (panel 2) and the ideal probability profiles (panel 3) of the three compartments. The bottom row shows the ideal profiles superimposed over the actual profiles. Notice the accurate correspondence. The discrepancy results from interpolation over the voxel lattice.

Figures 8 and 9 show a direct comparison of the Bayesian generated profiles (dashed line) and the hand generated profiles (solid line) of frequency of occurrence of white, gray, and CSF compartments as a function of distance from the gray/white matter boundary. Rows 1–4 of Fig. 8 show data from the prefrontal gyrus collected in the laboratory of Dr. Kelly Botteron of Washington University. Rows 1–3 of Fig. 9 show data from the cingulate gyrus from the laboratory of Dr. John Csernansky of Washington University. Row 4 shows data from the superior temporal gyrus.

Figure 10 shows the conditional probabilities of occurrence of white, gray, CSF compartments as a function of distance in mm from the gray/white matter boundary. The top row shows three prefrontal gyri analyzed from the laboratory of Dr. Kelly Botteron of Washington University. The bottom row shows two cingulate gyri and one superior temporal gyrus from the laboratory of Dr. John Csernansky of Washington University. Given the empirical probability distributions, the Bayes segmentation can be used with the informative prior distribution.

Errors in Surface Generation

To demonstrate the importance of the segmentation accuracy for surface generation, Fig. 11 shows an example where the method produces large and consistent errors. The top two rows show sections 10, 20, 30, 40, and 60 of the temporal gyrus of brain 1504. The top row shows the surface embedded in the image volume; the middle row shows the automated segmentation; and the bottom row shows details from sections 20, 40, and 60 with the embedded segmentation. Note that the automatically generated surface does not accurately correspond to the G/W boundary in several places. White matter falls outside the surface in the upper right corner of slice 20; gray matter falls inside the surface in the bottom center and elsewhere in slice 60.

The rightmost panel of the bottom row shows the resulting distance between the hand generated contour

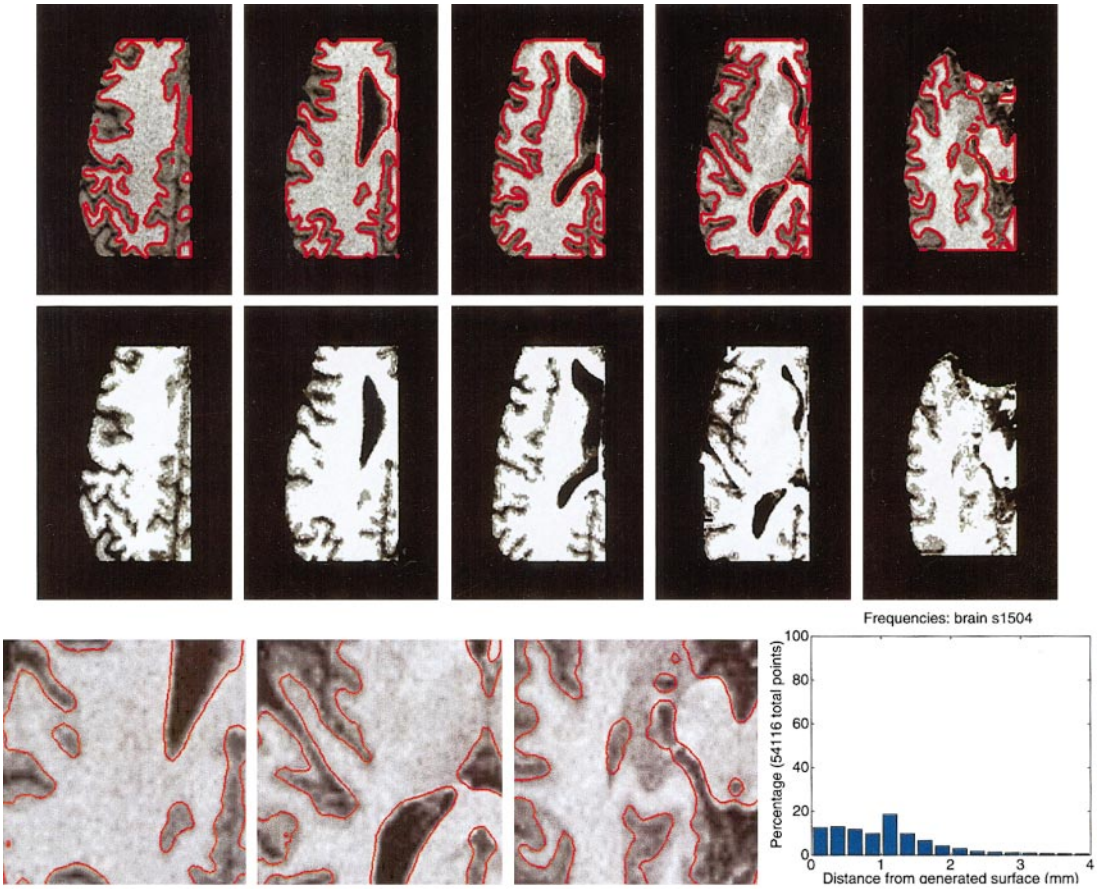

FIG. 11. Analysis of brain s1504 from the laboratory of Dr. John Csernansky. The top two rows show sections 10, 20, 30, 40, and 60, with the top row showing the surface embedded in the image volume and the second row showing the automated segmentation. The third row shows details from slices 20, 40, and 60 with the embedded segmentation. The graph at bottom right shows the L_1 distance between the hand-generated contour and the automatically generated surface for brain s1504. Compare this with the graphs in Fig. 6.

and the automatically generated surface for brain s1504. Compare this with the graphs in Fig. 6. Notice the spike in frequency at distance = 1 mm, corresponding to the greater discrepancy between the hand and auto generated surfaces for this brain. The error distance graph for brain s1504 directly reflects the flaws in the automatically generated surface, increasing our confidence in the surface validation procedure.

ACKNOWLEDGMENTS

We thank Dr. Hanna Damasio and Dr. Michael Vannier of the University of Iowa, for supplying us with the MRI data of the temporal gyrus and Lei Wang of Washington University for assistance with manual segmentations. This work has been supported by the NIH Grants R01-MH525158-01A1, R01-NS35368-02, R01-MH56584, and NSF BIR-9 424264, with partial support from Medtronic, Inc. and from the Mayo Foundation for the use of the Analyze software.

REFERENCES

Bakircioglu, M., Grenander, U., Khaneja, N., and Miller, M. 1998. Curve matching on brain surfaces using frenet distances. *Hum. Brain Mapp.* **6:** 329–332.

Bakircioglu, M., Joshi, S., and Miller, M. 1999. Landmark matching on brain surfaces via large deformation diffeomorphisms on the sphere. *Med. Imag. 1999: Image Process., Proc. SPIE* **3661,** 710–715.

Dale, A., and Sereno, M. 1993. Improved localization of cortical activity by combining EEG and MEG with MRI cortical surface reconstruction: A linear approach. *J. Cognit. Neurosci.* **5:** 162–176.

Drury, H. A., Essen, D. C. V., Anderson, C. H., Lee, C. H., Coogan, T. A., and Lewis, J. W. 1996. Computerized mappings of the cerebral cortex. A multiresolution flattening method and a surface-based coordinate system. *J. Cognit. Neurosci.* **8:** 1–28.

Essen, D. C. V., Drury, H., Joshi, S., and Miller, M. I. 1998. Functional and structural mapping of human cerebral cortex: Solutions are in the surfaces. *Proc. Natl. Acad. Sci. USA* **95:** 788–795.

Gueziec, A., and Hummel, R. 1995. Exploiting triangulated surface extraction using tetrahedral decomposition. *IEEE Trans. Vis. Comput. Graph.* **1:** 328–334.

Hurdal, M. K., Bowers, P. L., Stephenson, K., Sumners, D. W. L., Rehm, K., Schaper, K., and Rottenberg, D. A. 1999. Quasi-conformally flat mapping the human cerebellum. In *Lecture Notes in Computer Science* (C. Taylor and A. Colchester, Ed.), pp. 279–286. Springer-Verlag, Berlin.

Joshi, M., Cui, J., Doolittle, K., Joshi, S., Essen, D. V., Wang, L., and Miller, M. 1999. Brain segmentation and the generation of cortical surfaces. *NeuroImage* **9:** 461–476.

Kapur, T., Grimson, W., Wells-III, W., and Kikinis, R. 1996. Segmentation of brain tissue from magnetic resonance images. *Med. Image Anal.* **1:** 109–127.

Lorensen, W. E., and Cline, H. E. 1987. Marching cubes: A high resolution 3D surface construction algorithm. *Comput. Graph.* **21:** 163–169.

N. Khaneja, U., and Grenander, M. M. 1998. Dynamic programming generation of curves on brain surfaces. *Pattern Anal. Machine Intell.* **20:** 1260–1264.

Teo, P. C., Sapiro, G., and Wandell, B. A. 1997. Creating connected representations of cortical gray matter for functional MRI visualization. *IEEE Trans. Med. Imag.* **16:** 852–863.

Thompson, P., Schwartz, C., Lin, R., Khan, A., and Toga, A. 1996. Three-dimensional statistical analysis of sulcal variability in the human brain. *J. Neurosci.* **16:** 4261–4274.

Toga, A. W. 1999. *Brain Warping.* Academic Press, San Diego, CA.

Vaillant, M., and Davatzikos, C. 1997. Finding parametric representations of the cortical sulci using an active contour model. *Med. Image Anal.* **1:** 295–315.